WILEY | Hindawi

Research Article

Reservoir Temperature Calculation and Modeling for Convective Geothermal Systems: Case Study of Five Major Hot Springs in Lushan, Henan, China

Wang Qi,[1] Zhou Dongxu,[1] Liao Jiajia,[2] Liu Yuntao,[3] and Wang Xinyi [iD] [2,4,5]

[1]*College of Geosciences and Engineering, North China University of Water Resources and Electric Power, Zhengzhou 450045, China*
[2]*Institute of Resources & Environment, Henan Polytechnic University, Jiaozuo 454000, China*
[3]*Fifth Geological Exploration Institute of Henan Bureau of Geology and Mineral Exploration and Development, Zhengzhou 450045, China*
[4]*Collaborative Innovation Center of Coal Work Safety and Clean High Efficiency Utilization, Jiaozuo 454000, China*
[5]*Collaborative Innovation Center of Coalbed Methane and Shale Gas for Central Plains Economic Region, Jiaozuo 454000, China*

Correspondence should be addressed to Wang Xinyi; wangxy@hpu.edu.cn

The thermal storage temperature and water-rock interaction process of the Lushan convective geothermal system (Qinling stratigraphic zonation fracture zone in China) are clarified by using surface cold water and geothermal fluid as the research objects. In this study, a conceptual model of the temperature profile of the geothermal system in the study area was developed using surface temperature inversion, the cation temperature scale, the SiO_2 temperature scale method, the mineral equilibrium phase method, the silicon-enthalpy model, the FixAl method, and the Cl-enthalpy model. The inversion temperature at the surface is in the range of 33-39°C, and the temperature difference indicates the direction of the Checun-Lushan fracture. The study area is recharged from atmospheric precipitation, and the temperature of the recharge area is approximately 5.8–7.7°C (the temperature of the alkali field is approximately 10°C), and the recharge elevation is approximately 1200 m. The thermal storage pattern in the study area is near-surface hydrothermal thermal storage transferred to shallow thermal storage and then to deep thermal storage. The near-surface hydrothermal thermal storage temperature is at a constant temperature of 60°C, and the shallow thermal storage temperature is calculated by K-Mg and Li-Mg geothermometers to be between 99 and 112°C. The thermal storage temperature is simulated using the FixAl method, with deviation values ranging from 2.9% to 15.0%. The silicon-enthalpy model calculates the deep thermal storage temperature to be between 181 and 230°C. The mixing ratio of geothermal water in the study area is extremely high, with a cold water mixing ratio of 85.4–94.8%. The home ground fluid temperature was estimated to be approximately 282°C using the Cl-enthalpy model. The main thermally controlled conductivity channel in the study area is the Checun-Lushan fracture zone. The water vapor formed by convection at depth moves upward to approximately 5 km to form a deep thermal reservoir, and this convection and upward movement cause it to mix with cold water from the fracture zone to form a shallow thermal reservoir, which moves to the near-surface, forming a hydrothermal-type reservoir, which is later discharged in the form of a spring. The conceptual model of geothermal system temperature established in this study provides a basis for further development and utilization of Lushan hot springs and provides guidance for future thermal storage temperature calculations of convection-type geothermal systems in uplifted mountains.

1. Introduction

With global warming, the use of geothermal energy can help reduce environmental pollution and reduce the use of non-renewable resources [1, 2]. The main objectives of geothermal hydrogeochemical studies are to determine macronutrients, trace elements, and isotopes and investigate the source of geothermal water and its chemical

composition, geothermal storage temperature, hot and cold water mixing ratio, depth of geothermal water circulation, and the extent of water-rock reactions [3–11]. One of the main characterization elements of a geothermal system is the thermal storage temperature; the establishment of an analytical model of temperature can better visualize the causes of regional geothermal anomalies [12]. An early review of chemical reaction equilibria in geothermal systems was reported in New Zealand [13]. With the development of research on thermal reservoir temperature calculations, cationic thermometry has been heavily investigated to assess the thermal reservoir temperature of geothermal resources [14]. Different geothermometry methods have been proposed for water-rock interactions [15] (e.g., silica, isotope, rare gas, and trace element [10, 16–22]). Depending on the geothermal system, many studies have explored new methods based on the special local hydrogeological conditions to find more effective methods for thermal storage calculations [23, 24]. This should be a suitable study, but its ability to verify the applicability and generalizability of its thermal storage calculation requires further investigation.

Satellite remote sensing is a novel tool for detecting thermal anomalies in active volcanoes or hot spring areas [25]. Qin et al. [26] and Chan et al. [27] used the Landsat 7 satellite to perform thermal radiation inversions of the Tengchong area in Yunnan, China, and the Yilan Plain in northeastern Taiwan, respectively. Seward et al. [28] and Tian et al. [29] used Landsat 8 satellite thermal infrared data to evaluate surface temperatures in Taupo (Karapiti), New Zealand, and the geothermal field in Hokkaido, Japan. Using thermal radiation, geothermal activities, such as surface features, CO_2 sequestration [30], mineral assemblages [31], crater structures, and hot springs, have been shown to be detected.

During the study of thermal storage temperature calculations in geothermal systems, it was found that the dominant research methods have obvious limitations. Na-Li geothermometers have been proposed for volcanic and magmatic geothermal systems [32, 33] as well as for high-temperature geothermal fluids [34], and their main applicability is limited to geothermal anomalies with seawater intrusion.

Rare gas pyrometry is controlled in volcanic geothermal systems with high thermal reservoir temperatures and steam overflow [35]. Cation thermometry exhibits a positive and universal correlation with geothermal reservoir temperature, but there is a large deviation in low- and medium-temperature geothermal systems [36, 37], which may be due to the change in hydrothermal ion content caused by the large mixing of cold water in the region. In addition, several scholars have found that Na-K-Ca geothermometers are equally subjected to serious deviations in the calculation of thermal reservoir temperatures for low- and medium-temperature geothermal systems. It was found that the use of Na-K geothermometers can only be applied to geothermal systems with real thermal reservoir temperatures above 200°C [13]. Although correction of the Na-K-Ca geothermometer using the Mg correction method was later proposed by Giggenbach [38], Fournier [39], Chatterjee et al. [23], and Abdelali et al. [40], their calculation of thermal storage

temperature remains applicable only to a portion of the geothermal anomaly. In most studies of low-temperature geothermal systems, the K-Mg thermometer is currently used in preference to the Na-K-Ca geothermometer [41]. The Na-Li geothermometer method of [42] has also been used to estimate thermal storage temperatures in inland carbonate-based low-temperature geothermal systems.

Because geothermal water is mixed with cold water, it is difficult to reach the mineral dissolution equilibrium state, which is the main reason for the deviation of the majority of ion thermometers. The use of the silica-enthalpy model solves the mixing ratio of hot groundwater rising at a given depth to cold groundwater at the deep reservoir temperature [43] before mixing [39, 44]. The FixAl method has been applied extensively in recent years [45], using fixed Al to simulate the dissolution equilibrium convergence state of Al-containing minerals in hydrothermal fluids. As the Al value is low in the low- and medium-temperature geothermal systems, it may not be detected, and it is impossible to verify whether the fixed Al value is true and valid, leading to errors in the calculation of the thermal storage temperature of the low- and medium-temperature geothermal systems.

Pang and Reed and Tang and Pan [41, 46] initially explored the Lushan geothermal anomaly in 1984 and discussed the geothermal recharge mechanism in the study area, clarifying that the study area is an uplifted mountain-type convective geothermal system with a deep thermal storage temperature of approximately 90°C [47], and its ion geothermometer cannot characterize the accuracy of its thermal storage temperature owing to variations in the ion-water chemical ion content of geothermal water in the area. The objectives of this study are to (1) invert the surface temperature of the geothermal anomaly area using ENVI remote-sensing thermal radiography and (2) to clarify the recharge process of geothermal water and the main sources of recharge by using hydrogen and oxygen isotopes. The ion geothermometer method and mineral equilibrium phase method were used to deduce the thermal storage temperature of the shallow thermal reservoir in the study area. The FixAl method was used to simulate the thermal reservoir temperature and perform the deviation analysis. The deep thermal storage temperature and cold water mixing ratio in the study area were derived using the silicon-enthalpy model. The Cl-enthalpy model was used to estimate the temperature of the parent geothermal fluid. A conceptual model was established for the thermal storage temperature of the geothermal system in the study area. This study provides new insights into the temperature calculation of each reservoir in convective geothermal systems in the uplifted mountains.

2. Regional Geothermal Geological Background

2.1. Regional Geological Structure. Lushan in Henan Province is located on the upper reaches of the Shahe River in the Huaihe River system in the Shahe Valley of the Fuyu Mountains, which are an eastward extension of the Qinling Mountains. The elevation of the terrain is high in the west

and low in the east. The region is surrounded by mountains to the north, south, and west, with more than 30 peaks rising above 1000 m. It is connected to the Yellow Plain and Huai Plain in the east.

Along with the main ridge of Yao Mountain and other hilly landforms, the Checun-Xiatang fault and lateral erosion and undercutting by the Sha River have created a granite-dominated hilly landform 2.0 to 4.5 km wide along both banks of the Sha River, with low hills in the rest of the area. The hot springs overflow near the Sandy River and on relatively low-elevation first-order terraces.

Eruptive rocks of the middle Proterozoic Xionger Group and the Mesozoic Cretaceous Daying Group dominate the northern part of the study area. The main tectonic line is oriented almost east-west, with fracture structures spreading in a similar direction, and to the NE and NW (Figure 1). The near E-W fracture covers a large area and extends to considerable depth and consequently has the greatest heating influence in the region. The NE and NW fracture structures are small in scale but dense; in particular, the NE fractures occur in groups. These smaller fractures are responsible for secondary thermal control, thermal conductivity, and water storage. Tectonic joints, closely related to the small NE and NW faults, are also present in the area, often in dense zones on both sides of the small faults.

The primary lithology in the study area exhibits bedrock fracture water and loose rock-like pore water. Ejected rock crevice water is present in the area north of the Checun-Xiatang fault and southeast of the Zhaotai reservoir-alkali field. The intrusive rock crevice water is present in the fracture zone between the Checun-Xiatang, Erlangmiao-Wentangmiao, and Shuimozhuang-Licun faults. The fracture zone is strongly weathered along the tectonic fracture, and highly variable amounts of water are stored in the fractured and weathered rock. Pore water in loose rock occurs in the sand and pebble layers along the Shahe River and its tributaries and is also stored in the riverbed and on terraces. The terrain to the east of the Zhaotai Reservoir Dam is primarily an alluvial plain, and groundwater is stored in the sand and gravel layers.

2.2. Surface Temperature Inversion.

Anomalous surface temperatures and their extent are the most direct indicators of the presence of a regional geothermal zone, mainly detected by satellite remote sensing of surface infrared radiation. The intensity of water-rock mixing of near-surface groundwater is interpreted using the ENVI® 5.3 software.

In this study, the data source was a Landsat 8 Thematic Mapper (TM) satellite image of central China captured on September 31, 2021, at 03:03, selected as not being influenced by human activities. The real-time cloud content was 0.016. The image of the study area was radiometrically calibrated and atmospherically corrected (using the FLAASH atmospheric correction (QUAC) method) to obtain multispectral images and thermal infrared profiles of the study area (Figures 2(a) and 2(b)). The surface temperature inversion values were obtained by calculating the normalized difference vegetation index (NDVI), fractional vegetation (FV) cover, surface spectral emissivity (SSE), and blackbody emissivity (B(T)) of the study area.

The NDVI and FV were calculated for the study area using band calculation for input from Equation (1) and normalized by NDVI. In this study, ±2% was chosen as the upper and lower normalization thresholds. NDVI was calculated from

$$\text{NDVI} = \frac{(N.R.-R.)}{(N.R.+R.)}, \tag{1}$$

and F_V was then calculated from

$$F_v = \frac{(\text{NDVI}-\text{NDVI}_{min})}{(\text{NDVI}_{max} + \text{NDVI}_{min})}, \tag{2}$$

where $N.R.$ is the near-infrared visible reflectance, $R.$ is the visible reflectance, and $NDVI_{min}$ and $NDVI_{max}$ are the minimum and maximum values of $NDVI$ in the study area.

We substitute the image SSE calculation formula of the water body (SSE_w), natural surface (SSEN.S), and building surface (SSEB.S) into the band calculator of ENVI 5.3.

$$\text{SSE}_{W.} = 0.995, \tag{3}$$

$$\text{SSE}_{N.S.} = 0.9625 + 0.0614F_v - 0.0461F_{v2}, \tag{4}$$

$$\text{SSE}_{B.S.} = 0.9589 + 0.086F_v - 0.0671F_{v2}. \tag{5}$$

Blackbody radiance was calculated for the processed remote sensing spectral data, incorporating atmospheric correction parameters (atmospheric transmittance, atmospheric upward radiance, and atmospheric downward radiance). Inversion of the surface temperature in the study area was conducted using the inverse function of Planck's formula for blackbody radiation (Figure 2).

$$B(T) = \frac{[L\lambda - L\mu - \tau(1-\varepsilon)Ld]}{\tau \cdot \varepsilon}, \tag{6}$$

$$T = \frac{K_2}{\ln(K_1/B(T)+1)}, \tag{7}$$

where $L\lambda$ is the thermal infrared radiance brightness, ε is the surface radiance, $B(T)$ is the Planck thermal radiance brightness of a black body at temperature T, τ is the atmospheric transmittance, $L\mu$ is the atmospheric upward radiance brightness, and Ld is the atmospheric downward radiance brightness. τ, $L\mu$, and Ld were obtained from the NASA website for the specific imaging time and the latitude and longitude of the image center (33°45′43″ N, 112°44′49″ E); $\tau = 0.8$; $L\mu = 1.65$; and $Ld = 2.71$.

The surface temperature inversion pattern in Figure 2 clearly indicates four major geothermal temperature field anomalies in Shangtang (LS01), Zhongtang (LS04), Xiaotang (LS05), and Jianchang (LS07), whose temperature anomalies range between 33°C and 39°C. ArcGIS spatial information data comprise 155,587 spatial pixel points, of which temperatures of 33–39°C occupy 13% of the total study area and are
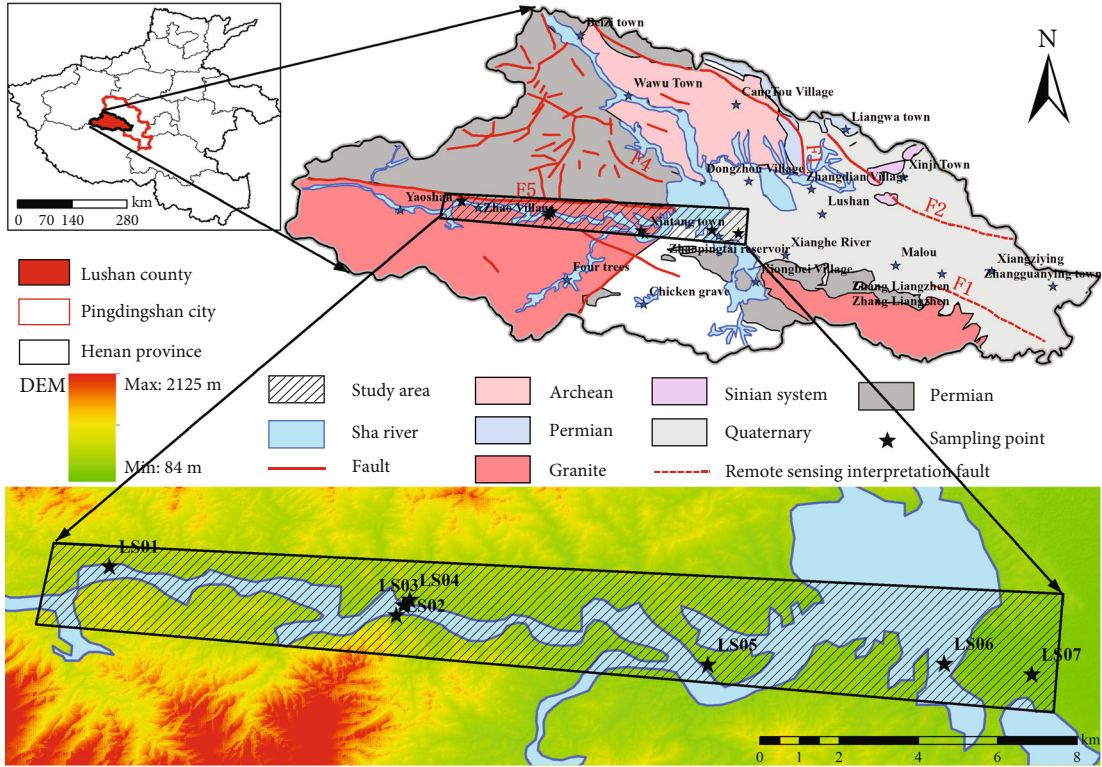
FIGURE 1: Location of the study area, showing basic geomorphology and coordinates of sampling points.
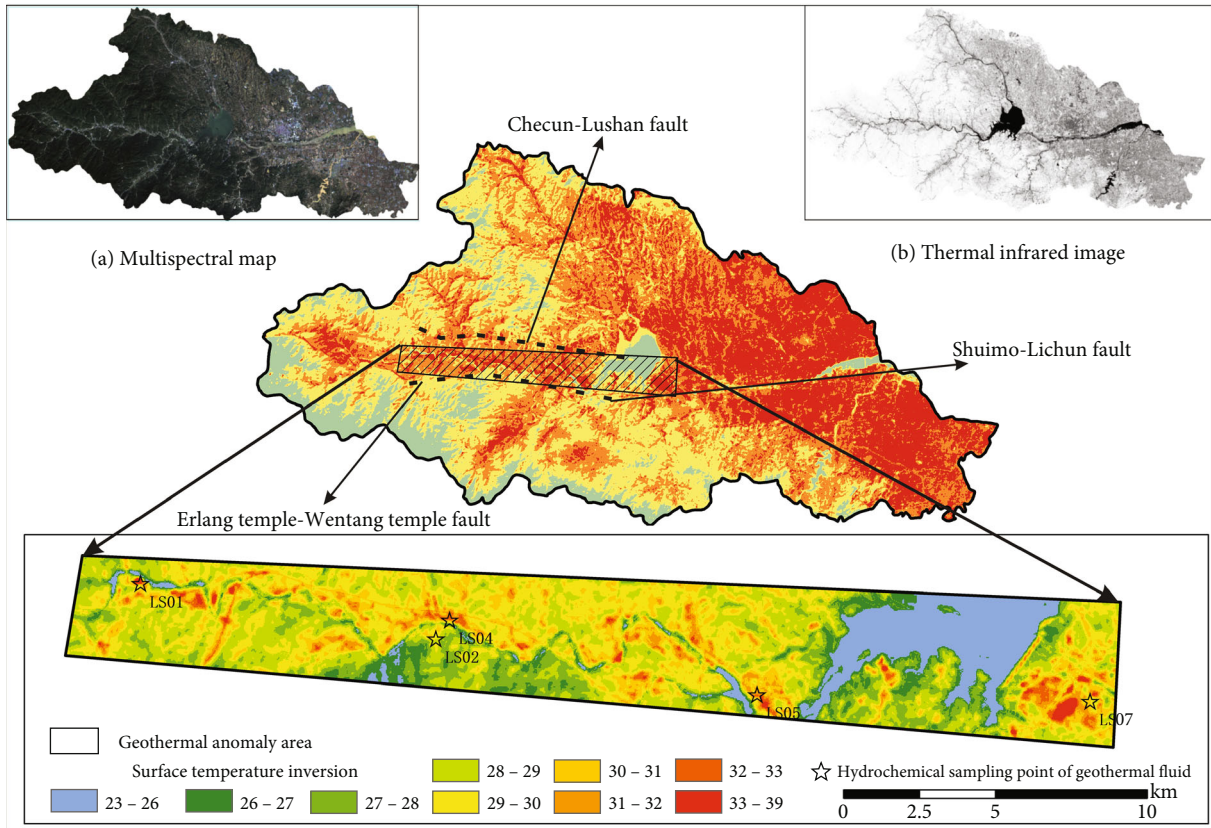

FIGURE 2: Surface temperature inversions in the geothermal anomaly area: (a) multispectral map of the study area (blue = band 1; green = band 2; red = band 3); (b) thermal infrared imaging map.

evident in small zones of anomalous temperatures. The temperature of the river water body is shown as 23–26°C (cf. 24.8–25.1°C for measured surface water samples), and the measured water temperatures at the five major geothermal hot spring sites were 36.7–47.6°C, validating the surface temperature inversion values. The large geothermal anomaly in the Jianchang area was due to the geothermal water being used for fish farming. The natural fishing pond is on the surface close to where geothermal water flows from the ground, directly exposing the geothermal water on the surface. The distribution of geothermal anomalies in Figure 2 implies that further geothermal anomalies may exist downstream of Shangtang, requiring further study.

Areas of obvious temperature difference are evident in the northern section of the study area, consistent with the location and orientation of the Checun-Lushan fault previously found in the course of the study (Figure 1). The traces of the Erlangmiao-Wentangmiao and Shuimozhuang-Licun faults in the southern area are also evident. These findings suggest that remote sensing would be appropriate in the future as a means of locating the spread of faults.

3. Materials and Methods

On October 25, 2021, seven sets of water samples (five sets of geothermal fluid water samples, one set of Shahe River water samples, and one set of drinking water source samples) were collected from west to east along the Checun-Lushan fault. The temperature, pH, electrical conductivity (EC), and total dissolved solids (TDS) of all samples were determined on-site using a WTW multiparameter water analysis tester (WTW Multi 3630 IDS, Germany). Measurement accuracies were, respectively, 0.1°C, 0.01 (for pH), 1 μS/cm, and 1 mg/L (see Figure 1 for the location of sampling points). Water samples for major ion analysis were filtered through 0.45 μm membrane filters into high-density polyethylene (HDPE) bottles, which had been washed in the field with the sampled water. Hydroxide isotope samples were collected in 100 mL glass vials (Table 1), sealed with plastic film, and stored at 4°C prior to laboratory analysis. The water samples were analyzed at the State Key Laboratory of China University of Geosciences (Wuhan); the hydrogen and oxygen isotope samples were analyzed at the State Key Laboratory of Henan University of Technology (incubation).

The main cations (Na$^+$, K$^+$, Mg^{2+}, Ca^{2+}, and Li$^+$) and anions (Cl$^-$, SO$_4^{2-}$, and F$^-$) were tested by ion chromatography (IC) using an iCAP 6300 spectrometer for inductively coupled plasma optical emission spectroscopy (ICP-OES) for cations and an 883 Basic plus IC for anions, with a detection limit of 0.0001 mg/L and precision of ±0.001 mg/L. The error in the water composition assessed by anionic charge balance was ±5%. HCO$_3^-$ concentrations were calculated using the PHREEQC software.

Oxygen and hydrogen isotopic compositions (δ^{18}O and δD) in the water were determined using a high-precision water isotope analyzer (Picarro L2140-i, USA). Each sample was analyzed three times to avoid the memory effect associated with the instrument. The results were reported in standard δ notation in per mille (‰) relative to the Vienna Standard Mean Ocean Water (VSMOW). The uncertainties of δ^{18}O and δD analyses were ±0.3‰ and ±1‰, respectively.

4. Results and Discussion

4.1. Hydrogen and Oxygen Isotope Characteristics

4.1.1. Water Source. The δD and δ^{18}O values indicate the source of recharge and the evolutionary pattern of the water body. In Table 2, the range of δD in the geothermal fluids is from −62.421‰ to −73.480‰ and δ^{18}O is from −7.523‰ to −9.247‰. The local atmospheric precipitation line hydrogen and oxygen stable isotopes were collected from the International Atomic Energy Agency (IAEA) website, and their local atmospheric precipitation curves were calculated by precipitation-weighted least-squares regression (PWLSR). Figure 3 shows the local meteoric water line (LMWL) given by δD = 7.9δ^{18}O + 8.2, the global meteoric water line (GMWL) δD = 8δ^{18}O + 10 [48], and the atmospheric precipitation line for Zhengzhou City, Henan Province, δD = 6.75δ^{18}O − 2.7, illustrating the hydrogen-oxygen isotope distribution.

The precipitation process line in Figure 3 for Pingdingshan fits the data well and was adopted as the local atmospheric precipitation process line. Figure 3 shows that local surface water and shallow groundwater are fully recharged by present-day atmospheric precipitation. The distribution of geothermal fluids in the study area appears to the lower left of the atmospheric precipitation process lines, indicating that the geothermal fluids in the study area are recharged by atmospheric precipitation, and that "oxygen drift" has occurred. This phenomenon indicates that during the flow of geothermal fluid, water-rock interaction leads to oxygen isotope exchange between the geothermal fluid and surrounding rocks, which enriches ^{18}O in the water. This situation indicates that atmospheric precipitation is the recharge source for the five major hot springs in the study area and that the long recharge path significantly increases the exchange of geothermal water with surrounding rocks during flow and transportation.

Because the δD and δ^{18}O values are affected by local temperature, elevation, and latitude, most studies currently apply the isotopic effects of atmospheric precipitation to obtain basic information about the geothermal fluids [48–50]. At present, the elevation effect in the North China Plain is to change the δ^{18}O value by −0.31‰ and δD by −1‰ to −4‰ for every 100 m of elevation [46]. Therefore, to take the elevation effect and latitude effect into account, the recharge elevation was calculated from

$$\delta D = -0.03\text{ALT} - 27, \tag{8}$$

$$H = \frac{h + (\delta G - \delta P)}{\text{grad } D}, \tag{9}$$

where ALT is the elevation of the recharge area (m), δD is the δD value at the sampling point (‰), h is the elevation of the sampling point (m), δG denotes the δD or δ^{18}O value

TABLE 1: Water chemistry and hydrogen-oxygen isotope data for the five major hot springs (mg/L).

Point	Shangtang	Zhongtang	Wentang	Xiatang	Jianchang	Sha River	Zhaopingtai reservoir
K^+	3.59	4.22	4.68	7.99	7.99	1.63	1.93
Na^+	131.95	129.2	150.35	132.65	185.05	11.34	6.18
Ca^{2+}	6.30	4.98	7.61	13.79	12.96	25.64	28.58
Mg^{2+}	0.12	0.09	0.19	0.84	0.32	3.45	4.71
Cl^-	24.65	25.36	24.55	35.65	48.61	6.31	7.04
SO_4^{2-}	124.62	94.36	130.64	117.53	154.28	29.25	28.53
HCO_3^-	186.78	186.84	203.62	203.37	254.13	118.34	84.424
F^-	15.02	15.8	12.98	15.53	10.34	0.96	0.20
NO_3^-	1.20	1.08	2.27	1.57	1.30	9.67	7.26
Li^+	0.13	0.23	0.23	0.41	0.25	–	0.01
SiO_2	29.615	34.095	29.285	31.665	28.3	7.027	5.304
δD	-71.623	-73.480	-68.038	-69.625	-62.421	-55.954	-58.053
$\delta^{18}O$	-9.179	-9.247	-8.613	-8.582	-7.523	-7.300	-7.398
TDS	658.5	652.7	779.8	652.7	695.6	209.7	875.2
pH	8.94	8.69	8.90	8.80	8.87	8.28	8.67

(– indicates that the ion content of the solution is not detected).

TABLE 2: Calculation of the recharge elevation (m) and temperature (°C) of the recharge area at the five major hot spring sites.

Num.	Point	δD	$\delta^{18}O$	Dem.	Equation (8)	Equation (9)	Average	Equation (10)	Equation (11)	Equation (12)	Average
LS01	Shangtang	-71.623	-9.179	275	1487.42	623.33	1055.38	6.362	5.058	6.883	6.10
LS04	Zhongtang	-68.038	-8.613	220	1367.94	580.03	973.99	7.176	5.697	10.097	7.66
LS02	Wentang	-73.48	-9.247	220	1549.33	638.14	1093.74	6.263	4.727	6.494	5.83
LS05	Xiatang	-69.625	-8.582	179	1420.83	628.71	1024.77	7.220	5.414	10.271	7.64
LS07	Jianchang	-62.421	-7.523	148	1180.68	595.13	887.91	8.744	6.699	16.292	10.58

at the sampling point (‰), δP is the δD or $\delta^{18}O$ of the atmospheric precipitation near the sampling point (‰), and grad D is the δD or $\delta^{18}O$ elevation gradient of atmospheric precipitation (2‰/100 m for the North China Plain).

The values of δD and $\delta^{18}O$ are positively correlated with the local temperature. Using this temperature effect, Dansgaard (1964) proposed a relationship between δD and $\delta^{18}O$ for the global mean annual precipitation and surface air temperature and a new set of equations for calculating the air temperature at the surface of the Earth.

$$\delta^{18}O = 0.695T - 13.6, \tag{10}$$

$$\delta D = 5.61T - 100, \tag{11}$$

$$\delta^{18}O = 0.176T - 10.39, \tag{12}$$

where T is the local annual average temperature (°C). $T = 14.8$°C in Lushan County.

In Table 3, Equation (8) gives a value approximately 800 m higher than Equation (9), which may be due to applying the gradient of the North China Plain for the study area, which is at a higher elevation; therefore, the mean value was adopted to improve the accuracy and place the elevation of the recharge area between 900 and 1100 m. The values calculated from Equations (10) and (12) are practically the same, but Equation (12) value is significantly higher than the

global temperature relationship curve, indicating that Equation (12) may be influenced by latitude. The Checun-Lushan fault is located at the lower edge of the stratigraphical boundary between northern China and Qinling. The elevation of the Qinling Mountains (located in the southwestern part of the study area) is above 1000 m. Therefore, based on the speculated recharge elevation, temperature, and topography of the recharge area, the groundwater recharge region within the study area is located in the mountainous area of Luonan County in the southeastern Qinling Mountains. The recharge path is a natural channel through the Luonan-Luanchuan-Chenshan-Gushi fracture structure (whose detailed location remains unknown).

4.2. Thermal Storage Temperature Calculation

4.2.1. Geothermometer Temperature Scale Method. Geothermometry is by far the most commonly used method of solving calculations for geothermal fluids. Na-K-Mg ternary diagrams are used to determine the ionic equilibrium and the state of water-rock action in geothermal aqueous solutions and to clarify the form of hydrothermal action affecting geothermal water in accordance with the CO_2 escape diagram proposed in [51] to determine the thermal storage temperature by a multicomponent type of geothermometry.

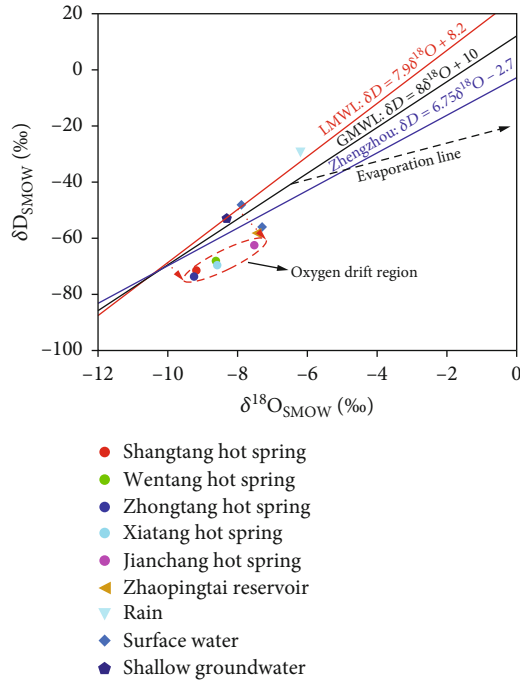Superimposing calcite dissolution from classical convective geothermal system theory to the Na-K-Mg ternary

FIGURE 3: Relationships between δD and $\delta^{18}O$ for the five major hot spring water samples in the study area. Rainwater and shallow groundwater isotope data are from measurements by the Henan Provincial Environmental Monitoring Center.

diagram for this study area (Figure 4(a)) [38] shows that the water-rock interaction of geothermal fluids in the study area is not in complete equilibrium, with the exception of Xiatang in the immature water zone. The other four geothermal sampling sites display a linear relationship, and their essentially constant Na-K concentration ratios indicate that the geothermal fluids in these four major geothermal fields are most likely sourced from the same thermal reservoir. This finding suggests that, in the study area, geothermal water is in a dilution process after it rises by convection. The dilution is consistent or subject to cold water mixing from the same recharge source, and thus the Na-K concentration ratio is not affected. Moreover, the boundary with the lower immature water deviates significantly from the equilibrium line, indicating that the Na-K and K-Mg ratios in its cationic geothermometer may show large deviations.

The Na-K-Mg combination in the geothermal fluids from the study area exhibits identical physicochemical properties to the geothermal water in the anomaly zone of the southeastern Yunnan fault, the Shenzhao geothermal field, and the Renkeng geothermal field. It differs greatly from the Xinzhou geothermal field in the coastal fracture area of Guangzhou. The Xiaotang and Renwu geothermal fields exhibit the same physicochemical properties; thus, it would be expected that the calculated Xiaotang thermal storage temperature would be consistent with that of the Renwu field. To clarify the differences between the geothermal fields, in this study, the equilibrium state of calcite dissolution in the study area and geothermal fields in the Tengchong area were further analyzed using the CO_2 escape diagram proposed in [38].

In Figure 4(b), the form of water-rock interaction in the study area differs significantly from the two geothermal fields in the Tengchong area. The geothermal water in Xiantang falls exactly on the granite dissolution curve. The other four geothermal waters are in complete equilibrium, and calcite has been fully formed. The water-rock interaction appears stronger than in the Na-K-Mg diagram, indicating the existence of degassing in the geothermal field. During the upward movement of geothermal water in the study area, the cold water is continuously diluted due to its density difference, and the ingested cold water is acidic granite warm water formed resulting from the limited residual heat of the acidic granite. The content of Na^+ and K^+ ions being transported is basically the same as in the geothermal water rising by convection, which is the reason for the linear relationship of Na-K in the four major geothermal waters in the Na-K-Mg ternary diagram.

Table 3 lists the results of the multicomponent geothermometric calculations, in which the calculated temperature approximates the actual temperature of the outlet water. This indicates that geothermometry is not applicable in this case and therefore cannot be used for reference. The calculated values for the Si temperature scale are lower than those for the cation temperature scale, probably due to large variations in the solubility of amorphous SiO_2 during the upward convective movement of the geothermal water [56]. It is notable that for the Na-K-Ca geothermometer in the study area, the Shangtang geothermal water does not satisfy the $\beta = 4/3$ condition, and the calculated results using the Mg-corrected method significantly deviate from the threshold range. It is also further shown that the Na-K-Ca- and Mg-corrected geothermometers do not perform well in low- and medium-temperature geothermal systems. The Na-Li thermometer is applicable to geothermal water mixed with seawater, and therefore, it is not used here [57, 58]. In this study, the Li-Mg and K-Mg geothermometers displayed values close to the thermal storage temperature in this study area (101–110°C for Li-Mg; 97–105°C for K-Mg), indicating that the thermal storage temperatures in the study area lie between 99°C and 112°C (approximate values: 100°C for Shangtang; 112°C for Zhongtang; 99°C for Xiatang; 104°C for Wentang; and 105°C for Jianchang).

4.2.2. Mineral Saturation Index Equilibrium Method. The mineral saturation index equilibrium method determines the overall chemical equilibrium state between hydrothermal fluids and minerals in a geothermal system by means of a multimineral equilibrium diagram [67]. The PHREEQC software based on equilibrium intervals was used to approach equilibrium at a given temperature simultaneously and to indicate if the hot water has reached equilibrium with this particular group of minerals. This was inferred from the temperature of the deep thermal storage of geothermal water. Based on the components of Yanshan-age granite in the study area, 10 reaction minerals (anhydrite, barite, celestite, chalcedony, dolomite, fluorite, quartz, sepiolite, $SiO_2(a)$, and strontianite iron ore) were selected in this study, and the temperatures were calculated at 20°C intervals from 60°C to 170°C for each of the five sampling points (Figure 5).

TABLE 3: Results from ion temperature scale method for five geothermal anomaly sampling points in the study area (unit: °C).

Geothermometer	Shangtang LS01	Zhongtang LS04	Xiatang LS05	Wentang LS02	Jianchang LS07	Data source
	80.21	92.15	138.90	88.91	112.09	
Na-K	103.33	116.47	168.25	112.9	138.50	Truesdell et al. [59]
	91.56	103.16	148.37	100.01	122.52	Amórsson et al. [60]
	114.93	125.32	164.70	122.51	142.37	
Mg-Li	101.37	119.32	105.05	110.03	104.20	Kharaka et al. [61, 62]
K-mg	97.36	104.56	92.24	98.10	105.53	Truesdell et al. [59]
Na-Li	148.34	176.25	210.60	169.32	161.72	Kharaka et al. [61, 62]
Na-K-ca, $\beta = 1/3$	123.86	132.97	153.60	130.02	143.67	Fournier[63]
Na-K-ca, $\beta = 4/3$	93.85	105.22	104.05	100.43	109.85	
Mg calibration, $\beta = 1/3$	189.65	140.44	554.06	295.14	277.50	Arnórsson and Andrésdóttir[64]
Mg calibration, $\beta = 4/3$	210.39	116.8	1016.81	383.21	345.42	
No vapor loss quartz type	78.87	84.76	81.64	78.41	77.02	Fournier [65]
Vapor loss quartz type	82.58	87.74	85.02	82.18	80.95	
No vapor loss chalcedony type	50.25	56.11	53.01	49.79	48.40	Amórsson and Andrésdóttir [64, 66]
Vapor loss chalcedony type	56.15	61.48	58.66	55.73	54.46	
Chalcedony type	47.50	53.71	50.42	47.01	45.54	Fournier [65]
α-Calcite	29.10	34.8	31.78	28.66	27.31	Fournier [39, 65]

Figure 5 shows the five major geothermal thermal storage temperatures as 143–160, 140–155, 152–165, 141–163, and 145–156°C, thus all grouped around 150°C. The highest temperature occurs at Xiatang, consistent with the geothermometrically calculated values. The five hot springs show a mineral saturation index (SI) of around −1, an indication that the major mineral phases are still in a dissolved state. As the mixed water is not fully exchanged with the hot surrounding rock during upward convective movement, it does not reach the equilibrium state of any of the minerals at any temperature. The geological structure in the study area is mainly Yanshan-age granites which mainly comprise quartz and other substances as well as feldspars and other minerals; thus, the SI deviation probably results from the absence of Al^{3+} ions, which makes it impossible to calculate the aluminosilicate mineral content. This situation possibly occurs if hot water mixes with shallow, cold water, and the unknown reacting mineral phase reinforces the inaccuracy of the dissolution equilibrium. The lack of Al^{3+} means that aluminosilicates do not become the generating mineral phase, which in turn affects the dissolution equilibrium state of the fluids.

For this reason, further exploration of the cold-water mixing ratio and Al^{3+} content of the five geothermal fields is required.

4.2.3. Silicon-Enthalpy Model.
To investigate the thermal storage temperature and the mixing of cold water with geothermal water in the study area, the silicon-enthalpy model was investigated in this study. Using the law of energy conservation, the initial enthalpy of the ratio of underground hot water mixed with cold water may be estimated from the local cold water temperature and its corresponding

SiO_2 content and the hot spring water temperature and its SiO_2 content. For ideal conditions,

$$S_c x + S_h(1 - x) = S_s, \tag{13}$$

$$SiO_{2c}x + SiO_{2x}(1 - x) = SiO_{2s}, \tag{14}$$

where S_c is the enthalpy of cold water, S_h is the enthalpy of geothermal water, S_s is the enthalpy of the hot spring, SiO_{2c} is the SiO_2 content of cold water (i.e., the measured SiO_2 content of the surface water sample, mg/L), SiO_{2x} is the content of SiO_2 in geothermal water (mg/L), and SiO_{2s} is the SiO_2 content of the hot spring (mg/L).

Figure 6 shows the thermal storage temperatures of the five major geothermal waters calculated by the silica-enthalpy model equation method: 230, 181, 217, 188, and 194°C, respectively. These are significantly higher than those calculated by geothermometric and mineral saturation equilibrium methods. Because the dissolved SiO_2 in the hot water deep underground is in a supersaturated state, the discharge temperature and the spring water SiO_2 contents are separate functions of the initial enthalpy of the hot water at depth. Moreover, the dissolution of SiO_2 in underground hot water follows the dissolution curve of quartz (lower temperature reduces SiO_2 solubility). Therefore, although the temperature of this hot water has been lowered, the SiO_2 in the supersaturated solution does not precipitate in a short time. Therefore, this method has wide application for calculating deep thermal storage temperatures. The mineral balance method gives deep thermal storage temperatures of approximately 140–160°C, but the minerals are still dissolved. This indicates that, at depth, the thermal storage temperature lies above this range. From this, it was deduced
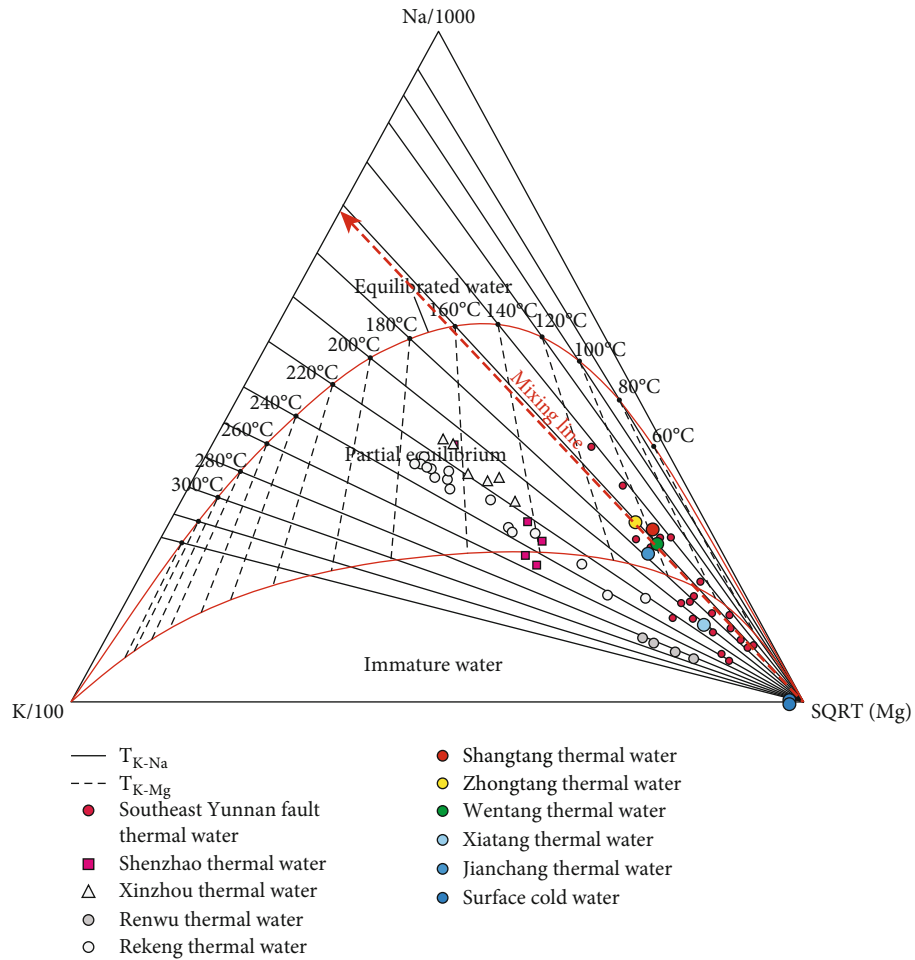
(a)
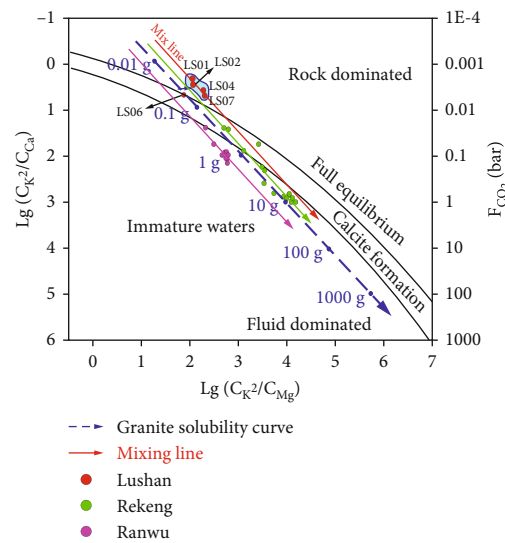
(b)

FIGURE 4: (a) Na-K-Mg ternary diagram of fractured deep-circulation-type geothermal water (Renwu, Rekeng from [52]; Shenzhao, Xinzhou from [53]; southeastern Yunnan Fault from [54]); (b) Ca, K, Mg, and CO_2 escape diagram in heated water [55]. Solid blue dots are the dissolution level of granite in 1000 g of water.
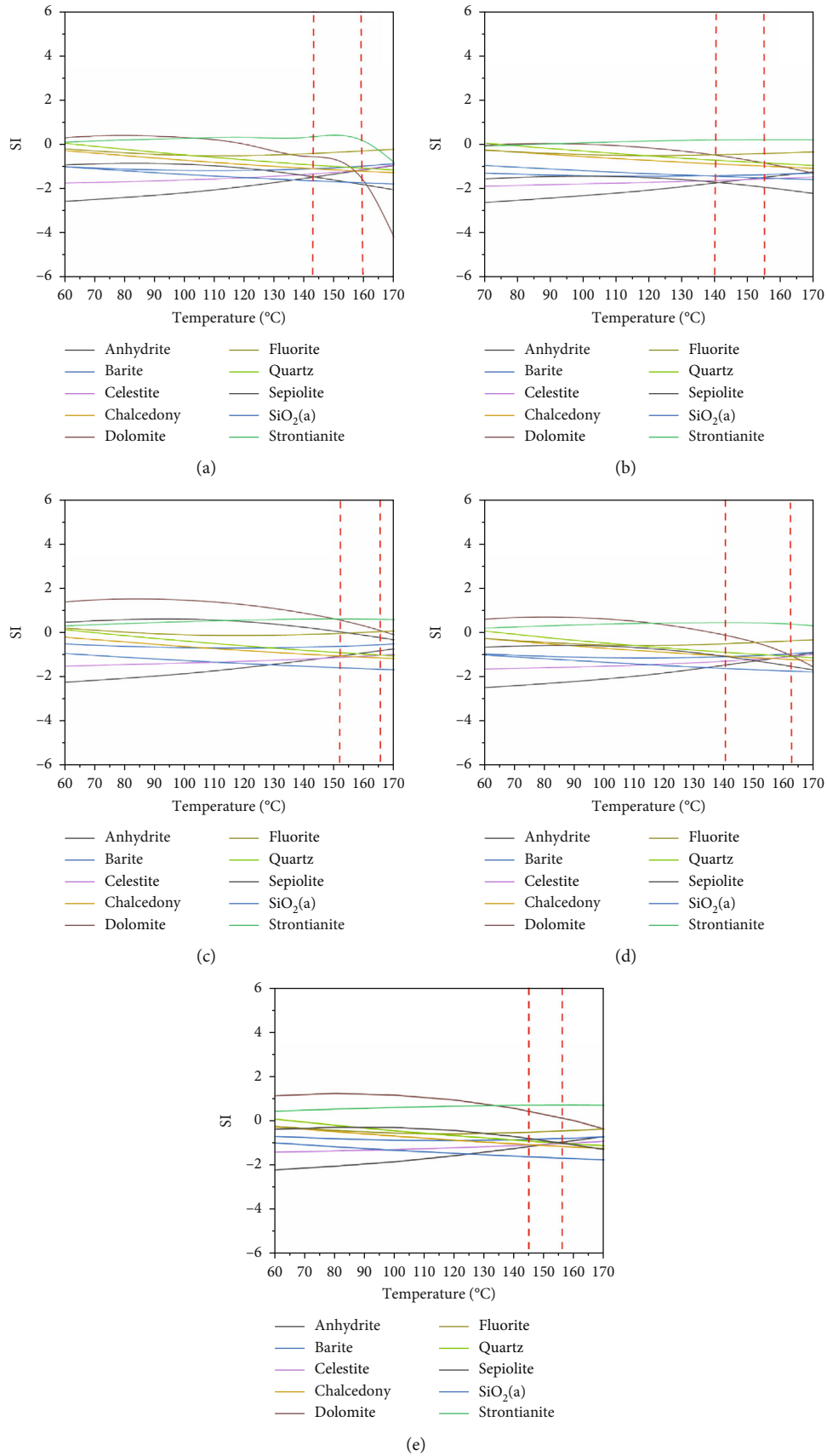
(a)

(b)

(c)

(d)

(e)

FIGURE 5: Zoning map for the mineral balance method for the five major hot springs: (a) Shangtang, (b) Zhongtang, (c) Xiatang, (d) Wentang, and (e) Jianchang.
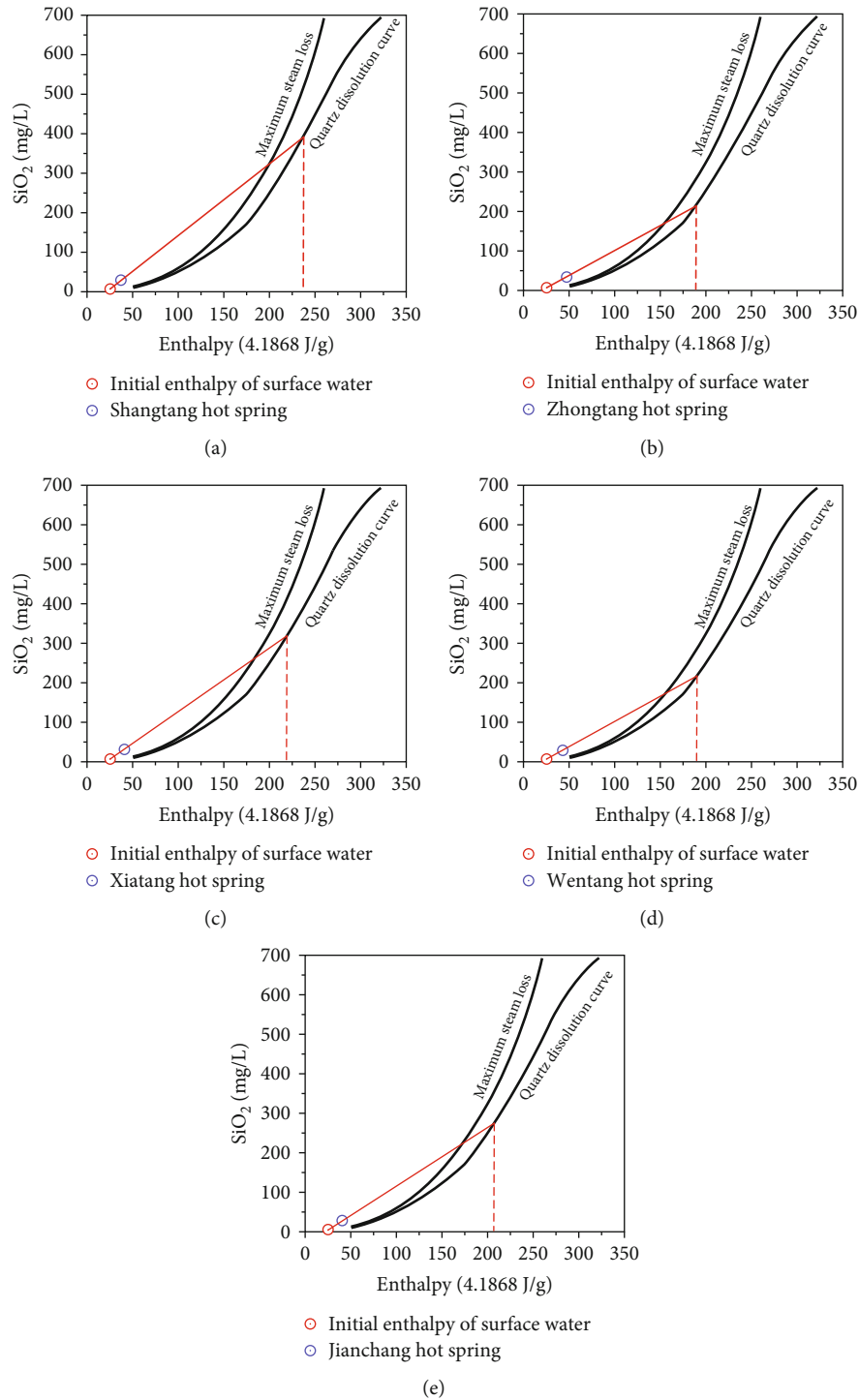
FIGURE 6: Silicon-enthalpy model graphical solution to the thermal storage temperature of the hot springs: (a) Shangtang, (b) Zhongtang, (c) Xiatang, (d) Wentang, and (e) Jianchang.

that the deep thermal storage temperature of the five major hot springs is between 181 and 230°C, the hottest being at Shangtang, followed by Xiatang.

The graphical solution for the cold-water mixing ratios of the five springs uses the cold-water mixing component of the silica-enthalpy model (Figure 7). The cold-water mixing ratios in this fractured geothermal anomaly area are extremely high, up to 94.8% in the Shangtang hot spring, 85.4% in Naktang, 92.2% in Shimotang, 88.7% in Winfield, and 90.8% in the Alkali field. Although many studies have concluded that convective geothermal systems in uplifted mountains are often associated with high cold-water mixing ratios, the very high values in this study area are probably the result of multiple cold-water mixing ratios.
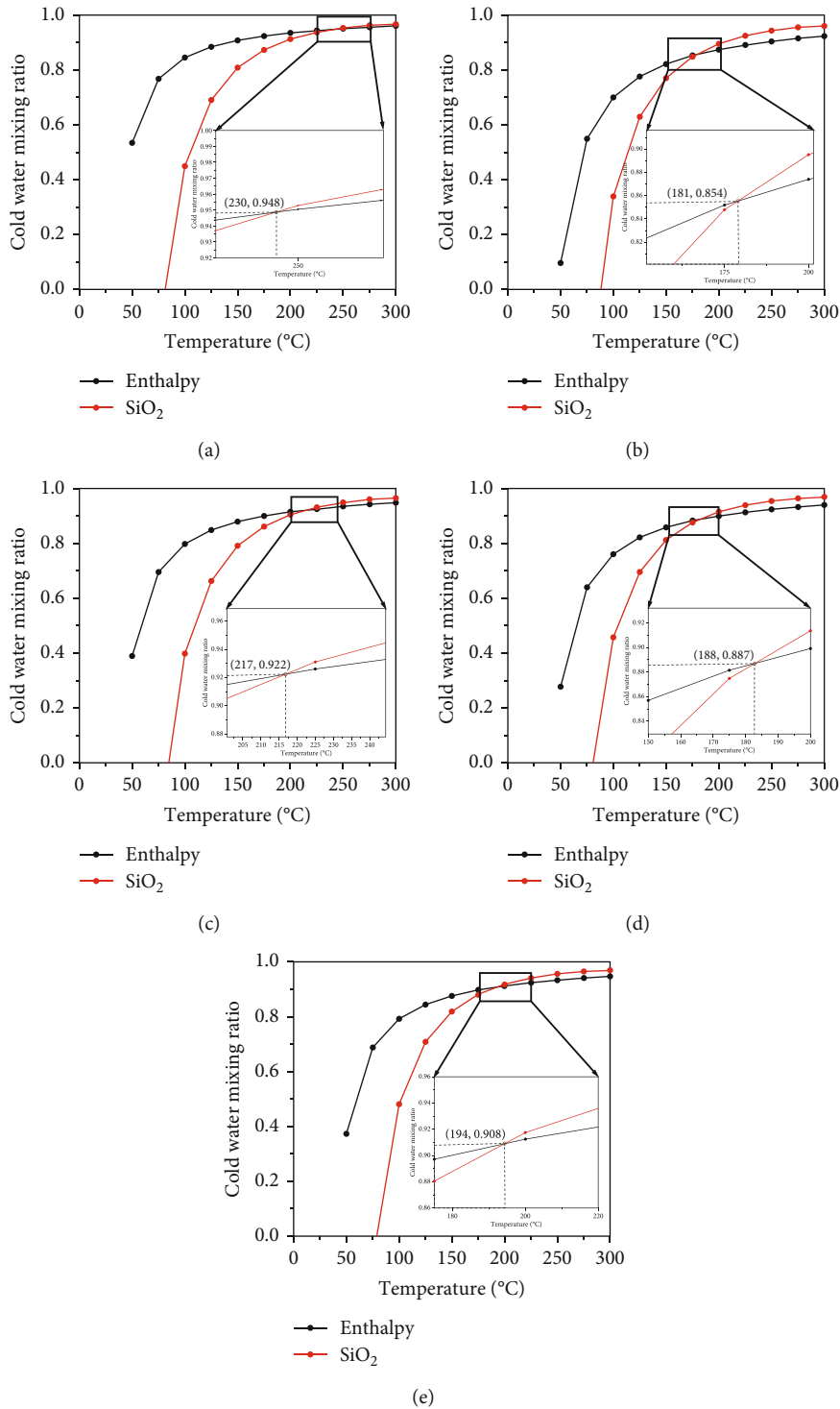
(a)

(b)

(c)

(d)

(e)

FIGURE 7: Silicon-enthalpy model to solve the cold water mixing ratio in the hot springs: (a) Shangtang, (b) Zhongtang, (c) Xiatang, (d) Wentang, and (e) Jianchang.

It is speculated, therefore, that the rapid upward flow along hydraulic fissures in the study area is due to the degassing of CO_2 and the consequent effect of air pressure. In addition, the presence of multiple layers of magmatic rock in the fracture zone subjects the geothermal fluid to this form of heat several times. The mixing of geothermal fluid with cold present-day water drops its temperature rapidly at a time when the water-rock interaction is extremely strong and the minerals remain in a relatively dissolved state and do not reach complete chemical equilibrium.

4.2.4. FixAl Method. Al^{3+} is the main ion in minerals in geothermal water, but it is often not detected during sampling and analysis owing to improper handling or low levels of
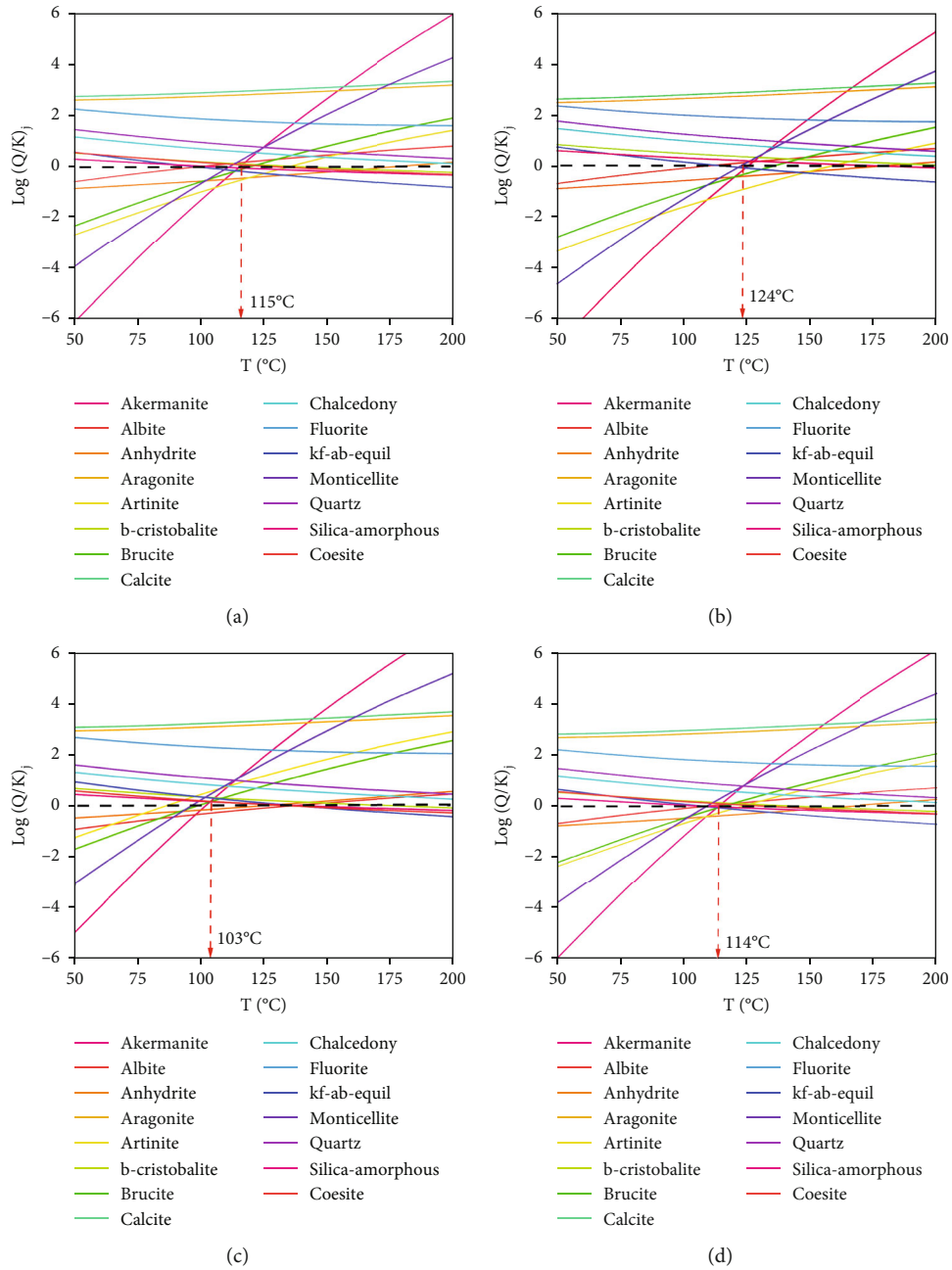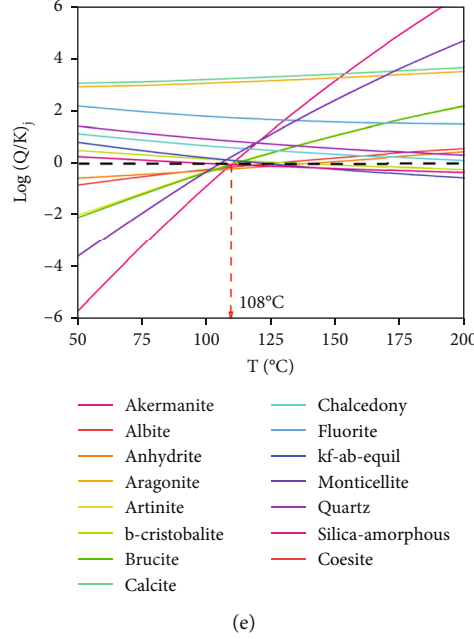
(a)

(b)

(c)

(d)

Figure 8: Continued.

(e)

FIGURE 8: Thermal storage temperature distribution of the five major hot springs using the FixAl correction method: (a) Shangtang, (b) Zhongtang, (c) Xiatang, (d) Wentang, and (e) Jianchang.

TABLE 4: FixAl corrected thermal storage temperature and conventional method calculation errors (unit: °C).

Point	Mg/Li-mg (average)	Mineral balance (average)	Silicon-enthalpy model	FixAl	Error (K-mg/Li-mg)	Error (mineral balance)	Error (silicon enthalpy)
LS01	100	157	230	115	+15.0%	-26.8%	-50.0%
LS04	112	148	181	124	+10.7%	-16.2%	-31.5%
LS05	99	164	217	103	+4.0%	-37.2%	-52.5%
LS02	104	152	188	114	+9.6%	-25.0%	-39.4%
LS07	105	151	194	108	+2.9%	-28.5%	-44.3%

TABLE 5: Results of circulation depths of five major geothermal water sites in the study area (unit: m).

Geothermal water point	Thermal storage depth (K-mg, Li-mg)	Thermal storage depth (silicon-enthalpy model)
Shangtang	1433	5947
Zhongtang	1833	4113
Xiatang	1400	5313
Wentang	1533	4347
Jianchang	1600	4547

the ion. Al^{3+} occurs in the main minerals in geothermal water (e.g., microcline, K-feldspar, and Na-feldspar). The FixAl method [68] enables the Al^{3+} content to be corrected and furthers the accurate assessment of the thermal storage temperature in the study area. The equilibrium of aluminosilicate minerals in geothermal systems is interactive; therefore, the Al^{3+} content can be estimated from the activity of Al^{3+} at different temperatures fixed by the interconstrained aluminous minerals. The activity product is calculated using the formula for the activity coefficient of Al-bearing minerals.

$$Q_k = \prod_{}^{i} a_{i,k}^{vi,k} = a_{Al}^{vAl,k} \prod_{}^{i-1} a_{m,k}^{vm,k}, \qquad (15)$$

where Q_k is the activity product of mineral k, $a_{i,k}$ is the activity of the hot water component, $v_{i,k}$ is the stoichiometric number of component I, and a_{Al} and $v_{Al,k}$ are the activity and stoichiometric number, respectively, of Al in mineral k.

Redefining Q_k and deriving Equation (15) for any one of the aluminum-containing minerals, j is obtained.

$$Q_{k,i-1} = \prod_{}^{i-1} a_{m,k}^{vm,k}, \qquad (16)$$

$$Q_k = a_{Al}^{vAl,k} Q_{k,i-1}, \qquad (17)$$

$$a_{Al} = \left(\frac{Q_j}{Q_{j,i-1}} \right)^{1/vAl,j}. \qquad (18)$$

After obtaining the activity of a_{Al}, forcing the mineral (microcline, the mineral in this study) to reach equilibrium
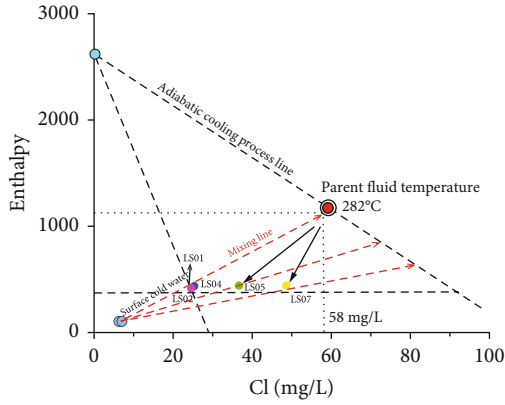
FIGURE 9: Cl-enthalpy diagram for the five major geothermal fluids.

with the aqueous solution fixes the activity of Al; thus, $Q_k = K_k$, giving the formula for $Lg(Q/K)j$.

$$Lg\left(\frac{Q}{K}\right)_j = Lg\left(\frac{K_k^S}{K_j}\right) - Lg\left(\frac{Q_{k,i-1}^S}{Q_{j,i-1}}\right). \qquad (19)$$

The H^+ content was solved for the measured temperature using the SOLVEQ-XPT software. At 50–200°C, the Al^{3+} activity and microplagioclase at 25°C reach dissolution equilibrium (i.e., SI = 0) for each mineral phase state, forcing the reaction-generated mineral phase to converge to a point with microcline. The converged value is the thermal storage temperature value of this geothermal field (Figure 8).

Figure 8 shows that, although the Al activity has been fixed in this reaction mineral phase, the convergent mineral phases of the five major geothermal springs do not converge well to the same point. With the change in temperature, the degree of dissolution change of SiO_2 is not obvious for mineral phases such as quartz and chalcedony, whereas carbonate rock minerals such as calcite deviate from the dissolution equilibrium line and their phases are in a fully formed state. This phenomenon is in full agreement with the conclusion of Figure 4(b). The thermal storage temperatures of the five major hot springs converge at 115, 124, 103, 114, and 108°C. The comparison reveals that the temperature obtained by the FixAl correction method more closely approximates the calculated result of the cationic temperature scale. However, for Xiatang, the Al-containing silicate mineral phase converges ahead of the SiO_2 mineral phase, indicating that the nature of SiO_2 does not change significantly with temperature, but the degree of dissolution of amorphous SiO_2 is practically the same as for the Al silicate minerals. This conclusion is consistent with the difference in geothermal temperature scale calculation in Li. [56].

The thermal storage temperatures derived by the FixAl method differ from those of the cation temperature scale, mineral equilibrium simulations, and silica-enthalpy models (Table 4). As Table 4 shows, the FixAl method describes the thermal storage temperature values of the low- and medium-temperature types to a certain extent, and its simulated calculated thermal storage temperature is within the 2.9–15% range of the calculated error of the cationic temperature

scale method. The simulated ions did not include the Li^+ content, and the small magnitude of the error is sufficient to show that the FixAl method is able to specify the same thermal storage temperature as the Li-Mg geothermometer.

The FixAl method may be used to directly verify the applicability of the mean value of the K-Mg and Li-Mg geothermometers for shallow thermal storage calculated in this study. Similarly, the SiO_2 convergence indicates the inapplicability of the silica temperature scale in the study area. It also provides a reciprocal theory for the solution of the thermal storage temperature problem for low- and medium-temperature types of convection.

4.3. Circulation Depth. The depth of groundwater circulation is an important parameter in determining the renewal rate and exploration of recharge and runoff properties of the groundwater system. The geothermal fluid in the Checun-Lushan fault anomaly area is mainly influenced by the fracture structure, and its circulation depth is related to the depth of the hydraulic conduction fracture. Therefore, the formula for circulation depth for geothermal water is, at present, the most effective way of determining the depth of a thermal reservoir:

$$D = \frac{(T_H - T_S)}{\Delta t} + h, \qquad (20)$$

where D is the circulation depth (m), T_H is the calculated thermal-storage temperature (°C), T_S is the surface cold-water temperature (°C), Δt is the geothermal warming gradient (°C/100 m) (the Chinese geothermal heat flow database collection of Henan Province gives 3°C/100 m), and h is the thickness of the normal temperature layer (m), generally 20 m.

According to Table 5, the burial depth of shallow thermal storage in the study area is approximately 1.5 km using the Li-Mg and K-Mg geothermometers, and the burial depth is approximately 5 km using the silicon-enthalpy model. The depth of the Checun-Lushan fracture is 5.2 km, and its fracture depth is consistent with the calculation of the burial depth of deep thermal storage. It is clear from the depth of thermal storage that the Checun-Lushan fracture zone in the north of the study area is the main heat-control and heat-conducting channel, and the secondary fracture zones in the northwest and northeast play a role in blocking the water vapor formed by convection; thus, a shallow thermal storage layer is formed 1.5 km above the line and finally discharged in the form of a spring.

4.4. Estimation of Parent Fluid Temperature. The Cl-enthalpy diagram [69] describes in detail the various cooling processes that the geothermal fluid undergoes during upflow and enables the temperature of its parent geothermal fluid to be obtained (Figure 9). Substituting the results of the K-Mg and Li-Mg geothermometer calculations, the geothermal fluid flow in the study area from west to east, the lower immature water, and the alkali field geothermal water experienced significant degassing. This also indicates that a longer reaction path produces a stronger hydration reaction
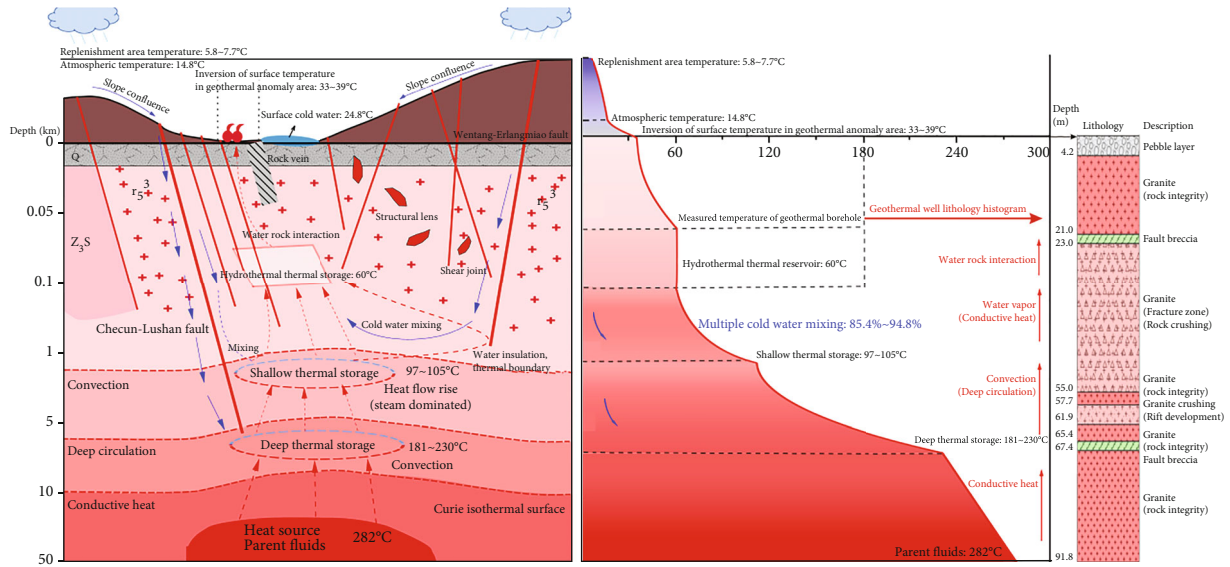
FIGURE 10: Conceptual temperature model of a convective geothermal system in the study area (left: geothermal genetic model of the study area profile, middle: thermal reservoir temperature curve, right: lithologic histogram of Shangtang Hot Spring).

effect after contact with the surrounding rock and increases the likelihood of water-rock interaction. In Figure 9, the parent geothermal fluid thermal temperature in the study area is approximately 282°C, and its Cl^{-} content is around 58 mg/L. This provides a reference for the thermal storage temperature of the parent geothermal fluid in the study area.

4.5. Stratified Thermal Storage Model. Based on the preliminary geothermal well-water survey and borehole histogram (Figure 10), the water temperature in the study area within 60 to 100 m is always 60°C, and the geothermal gradient is zero. This indicates that the shallow thermal reservoir temperature is not caused by geothermal warming but results from the transport and enrichment of hot water from the deep to shallow region, such that 60°C (in the present case) is the balanced water and rock temperature. Therefore, to calculate circulation depth, a new method is proposed for the study area. It uses existing equations but substitutes the hydrothermal storage temperature of the geothermal wells for the cold water temperature Ts near the surface, and the measured shallow thermal storage depth is the thickness, h, of the normal temperature layer. Then, the circulation depth is calculated using the geothermometer method and the thermal storage temperature of the silica-enthalpy model.

Because cold modern water mixing occurs several times, the temperature of the geothermal fluid is reduced significantly. In most current studies, the thermal storage calculation primarily focuses on the parent fluid, deep thermal storage temperature, and effluent temperature; however, for geothermal systems in particular geological formations, it is obvious that the model of parent fluid → deep thermal storage → effluent temperature is not the best explanation of thermal storage temperature. Therefore, it appears that a shallow thermal storage + deep thermal storage model is appropriate in the geothermal area covered in this study.

The model indicates that the parent ground fluid temperature of 282°C transports the heat source to the upper area by conduction, and the Chechon-Lushan fracture provides a channel for water conduction from approximately 5.5 km depth; this also provides a mixing channel. Deep convective circulating geothermal water reaches the deep thermal storage temperature, calculated here by the silicon-enthalpy model to be 181–230°C. When the geothermal water reaches this temperature, water vapor moves upward due to CO_2 degassing, and during its upward transport through the faulted hydraulic channel, it mixes with so-called "cold" water from the fracture zones of magmatic intrusive rocks. The cold water is heated to a particular temperature by exothermic residual heat from magmatic intrusive rocks as it interacts with the rock. The groundwater mixed with the rising hot geothermal fluid eventually reaches a shallow thermal storage temperature of 99–112°C at approximately 1.5 km below the surface. The geothermal water is transported upward by drainage and is heated to the same temperature as the surrounding rock reservoir near the surface. At the same time, due to the high water content of the fractured zones in tectonically developed reservoirs, hydrothermal thermal storage forms near the surface. It subsequently overflows onto the ground surface as a hot spring.

The stratified thermal storage model in this study, together with a temperature process profile of convective type in uplifted mountains, was established by combining into one vertical spatial dimension, the temperature of the recharge area, atmospheric temperature, surface anomaly temperature, hydrothermal-type thermal storage temperature, shallow thermal storage, deep thermal storage, and Earth fluid temperature (Figure 10). This model contains implications for the direction of future studies of thermal storage temperature calculations in fractured, convection-type geothermal anomalies.

5. Conclusions

(1) The surface temperature in the geothermal anomaly area is between 33° and 39°C. The strikes of the Checun-Lushan, Erlangmiao-Wentangmiao, and Shuimozhuang-Licun faults at the northern and southern sides of the study area are clearly shown by the differences in surface temperature, and a new research tool for future fracture orientation is provided

(2) Hydrogen and oxygen isotope data indicate that the study area is recharged through atmospheric precipitation with a long recharge path and a recharge zone temperature of 5.8–7.7°C, with the recharge temperature of the alkali plant at approximately 10°C. The recharge elevation exceeds 1100 m

(3) There is a near-surface hydrothermal thermal reservoir with a temperature of 60°C near the surface of the study area. The study area has a "shallow thermal storage + deep thermal storage" model. The shallow thermal storage temperatures of the five hot springs are 100, 112, 99, 104, and 105°C. The silica-enthalpy model analysis shows that the cold water mixing ratio in the study area is extremely high, ranging from 85.4% to 94.8%. The deep thermal storage temperature was calculated to be between 185 and 230°C. In addition, the mineral equilibrium method extrapolates the thermal storage temperature in such a way that the mineral phase cannot reach the dissolved equilibrium state; therefore, there is an error. The results indicate that the cationic temperature scale and mineral equilibrium method are greatly influenced by cold water mixing

(4) Despite the lack of Al data, the FixAl method found that most of the Al-containing minerals could converge by fixing the Al value at 0.005 mg/L while specifying an error of 2.9% to 15% with the cationic temperature scale

(5) The study area has the thermal storage mode of shallow thermal storage + deep thermal storage. Analysis of the Cl-enthalpy diagram indicated that the Cl content of the parent geothermal fluid is approximately 58 mg/L, and the temperature of the parent geothermal fluid thermal storage is around 282°C. Therefore, a conceptual model was established for the thermal storage temperature of geothermal systems, providing a new understanding of the thermal storage calculation of a convective geothermal system in uplifted mountains

Data Availability

The data used to support the findings of this study are included within the article.

Conflicts of Interest

The authors declare that they have no conflicts of interest.

References

[1] A. F. Bayram, "Hydrogeochemistry and geothermometry of the Ilgin geothermal field, Central Turkey," *Island Arc*, vol. 32, no. 1, article e12478, 2023.

[2] G. Feng, Y. Wang, T. Xu, F. Wang, and Y. Shi, "Multiphase flow modeling and energy extraction performance for supercritical geothermal systems," *Renewable Energy*, vol. 173, pp. 442–454, 2021.

[3] A. M. S. Altaş and Ü. Gemici, "Hydrogeochemical pattern and environmental isotope hydrology of coastal Bademli geothermal area (BGA) in western Turkey (Dikili-İzmir): a new geothermal prospect," *Turkish Journal of Earth Sciences*, vol. 32, no. 1, pp. 113–125, 2023.

[4] A. Dutta, A. P. Thapliyal, P. K. Singh, S. Rohilla, and R. K. Gupta, "Geological setup and physicochemical characteristics of Munger Groups of thermal springs along Munger–Saharsa Ridge Fault, Bihar, India: a conceptual hydrogeochemical model," *Journal of Earth System Science*, vol. 132, no. 1, p. 12, 2023.

[5] J. Wang, X. Zhou, M. He et al., "Hydrogeochemical origin and circulation of spring waters along the Karakorum fault, Western Tibetan Plateau: implications for interaction between hydrosphere and lithosphere," *Frontiers in Earth Science*, vol. 10, article 1021550, 2022.

[6] Y. Liao, Y. Liu, G. Wang et al., "Genesis mechanisms of geothermal resources in Mangkang geothermal field, Tibet, China: evidence from Hydrochemical characteristics of geothermal water," *Water*, vol. 14, no. 24, p. 4041, 2022.

[7] X. Yu, C. Liu, C. Wang, J. X. Zhao, and J. Wang, "Origin of geothermal waters from the upper cretaceous to lower Eocene strata of the Jiangling Basin, South China: constraints by multi-isotopic tracers and water-rock interactions," *Applied Geochemistry*, vol. 124, p. 104810, 2021.

[8] X. Wang, T. Xia, L. Zhang, Z. Ding, S. He, and Y. Peng, "Effect of soil microstructure on the small-strain shear modulus of saline soil," *Arabian Journal of Geosciences*, vol. 14, no. 1, p. 1, 2021.

[9] A. Davraz, M. T. Nalbantçılar, and İ. Önden, "Hydrogeochemical characteristics and trace element of geothermal systems in Central Anatolia, Turkey," *Journal of African Earth Sciences*, vol. 195, article 104666, 2022.

[10] D. J. Byrne, M. W. Broadley, S. A. Halldórsson et al., "The use of noble gas isotopes to trace subsurface boiling temperatures in Icelandic geothermal systems," *Earth and Planetary Science Letters*, vol. 560, article 116805, 2021.

[11] F. Yu, D. Zhou, Z. Li, and X. Li, "Hydrochemical characteristics and hydrogeochemical simulation research of groundwater in the Guohe River Basin (Henan section)," *Water*, vol. 149, no. 9, pp. 1461–1475, 2022.

[12] H. Wang, Z. Kou, J. Guo, and Z. Chen, "A semi-analytical model for the transient pressure behaviors of a multiple fractured well in a coal seam gas reservoir," *Journal of Petroleum Science and Engineering*, vol. 198, p. 108159, 2021.

[13] A. J. Ellis, "Quantitative interpretation of chemical characteristics of hydrothermal systems," *Geothermics*, vol. 2, pp. 516–528, 1970.

[14] A. Rezaei, M. Rezaeian, and S. Porkhial, "The hydrogeochemistry and geothermometry of the thermal waters in the Mouil Graben, Sabalan volcano, NW Iran," *Geothermics*, vol. 78, pp. 9–27, 2019.

[15] Z. Kou, H. Wang, V. Alvarado et al., "Effects of carbonic acid-rock interactions on CO_2/brine multiphase flow properties in the upper Minnelusa sandstones," *SPE Journal*, vol. 28, no. 2, pp. 754–767, 2023.

[16] H. Aydin, H. Karakuş, and H. Mutlu, "Hydrogeochemistry of geothermal waters in eastern Turkey: geochemical and isotopic constraints on water-rock interaction," *Journal of Volcanology and Geothermal Research*, vol. 390, p. 106708, 2020.

[17] S. Elidemir, N. Güleç, K. Deniz, and Y. K. Kadıoğlu, "Reservoir rock characterization in Edremit geothermal field: geochemical implications for possible fault zones," *Applied Geochemistry*, vol. 143, p. 105388, 2022.

[18] B. Capaccioni, O. Vaselli, F. Tassi, A. P. Santo, and A. D. Huertas, "Hydrogeochemistry of the thermal waters from the Sciacca geothermal field (Sicily, southern Italy)," *Journal of Hydrology*, vol. 396, no. 3–4, pp. 292–301, 2011.

[19] Y. Cui, C. Zhu, N. Qiu, B. Tang, and S. Guo, "Radioactive heat production and terrestrial heat flow in the Xiong'an area, North China," *Energies*, vol. 12, no. 24, p. 4608, 2019.

[20] T. L. Harley, R. Westaway, and A. T. McCay, "Gamma-ray spectrometry in the field: radioactive heat production in the central Slovakian volcanic zone," *Journal of Volcanology and Geothermal Research*, vol. 338, pp. 1–24, 2017.

[21] T. Xu, Z. Hou, X. Jia et al., "Classical and integrated multicomponent geothermometry at the Tengchong geothermal field, southwestern China," *Environmental Earth Sciences*, vol. 75, no. 24, pp. 1–10, 2016.

[22] Z. Hou, T. Xu, S. Li et al., "Reconstruction of different original water chemical compositions and estimation of reservoir temperature from mixed geothermal water using the method of integrated multicomponent geothermometry: a case study of the Gonghe Basin, northeastern Tibetan Plateau, China," *Applied Geochemistry*, vol. 108, p. 104389, 2019.

[23] S. Chatterjee, U. K. Sinha, B. P. Biswal, A. Jaryal, S. Patbhaje, and A. Dash, "Multicomponent versus classical geothermometry: applicability of both geothermometers in a medium-enthalpy geothermal system in India," *Aquatic Geochemistry*, vol. 25, no. 3-4, pp. 91–108, 2019.

[24] C. C. Harvey, G. R. Beardsmore, I. Moeck et al., *Geothermal Exploration: Global Strategies and Applications*, IGA Academy, 2016.

[25] M. B. Mia, Y. Fujimitsu, and J. Nishijima, "Exploration of hydrothermal alteration and monitoring of thermal activity using multi-source satellite images: a case study of the recently active Kirishima volcano complex on Kyushu Island, Japan," *Geothermics*, vol. 79, pp. 26–45, 2019.

[26] Q. Qin, N. Zhang, P. Nan, and L. Chai, "Geothermal area detection using Landsat ETM+ thermal infrared data and its mechanistic analysis–a case study in Tengchong, China," *International Journal of Applied Earth Observation and Geoinformation*, vol. 13, no. 4, pp. 552–559, 2011.

[27] H. P. Chan, C. P. Chang, and P. D. Dao, "Geothermal anomaly mapping using Landsat etm+ data in Ilan plain, northeastern Taiwan," *Pure and Applied Geophysics*, vol. 175, no. 1, pp. 303–323, 2018.

[28] A. Seward, S. Ashraf, R. Reeves, and C. Bromley, "Improved environmental monitoring of surface geothermal features through comparisons of thermal infrared, satellite remote sensing and terrestrial calorimetry," *Geothermics*, vol. 73, pp. 60–73, 2018.

[29] B. Tian, L. Wang, K. Kashiwaya, and K. Koike, "Combination of well-logging temperature and thermal remote sensing for characterization of geothermal resources in Hokkaido, northern Japan," *Remote Sensing*, vol. 7, no. 3, pp. 2647–2667, 2015.

[30] Z. Kou, H. Wang, V. Alvarado, J. Fred McLaughlin, and S. Austin Quillinan, "Method for upscaling of CO_2 migration in 3D heterogeneous geological models," *Journal of Hydrology*, vol. 613, p. 128361, 2022.

[31] Z. Kou, D. Zhang, Z. Chen, and Y. Xie, "Quantitatively determine CO_2 geosequestration capacity in depleted shale reservoir: a model considering viscous flow, diffusion, and adsorption," *Fuel*, vol. 309, p. 122191, 2022.

[32] G. Michard, "Behaviour of major elements and some trace elements (Li, Rb, Cs, Sr, Fe, Mn, W, F) in deep hot waters from granitic areas," *Chemical Geology*, vol. 89, no. 1–2, pp. 117–134, 1990.

[33] G. Michard and E. Roekens, "Modelling of the chemical composition of alkaline hot waters," *Geothermics*, vol. 12, no. 2–3, pp. 161–169, 1983.

[34] E. Santoyo and L. Díaz-González, "A new improved proposal of the Na/K geothermometer to estimate deep equilibrium temperatures and their uncertainties in geothermal systems," in *Proceedings of the World Geothermal Congress*, Bali, Indonesia, April 2010.

[35] V. Roche, V. Bouchot, L. Beccaletto et al., "Structural, lithological, and geodynamic controls on geothermal activity in the Menderes geothermal province (Western Anatolia, Turkey)," *International Journal of Earth Sciences*, vol. 108, no. 1, pp. 301–328, 2019.

[36] F. Nitschke, S. Held, T. Neumann, and T. Kohl, "Geochemical characterization of the Villarrica geothermal system, Southern Chile, part II: site-specific re-evaluation of SiO_2 and Na-K solute geothermometers," *Geothermics*, vol. 74, pp. 217–225, 2018.

[37] J. Li, G. Sagoe, G. Yang, and G. Lu, "Evaluation of mineral-aqueous chemical equilibria of felsic reservoirs with low-medium temperature: a comparative study in Yangbajing geothermal field and Guangdong geothermal fields," *Journal of Volcanology and Geothermal Research*, vol. 352, pp. 92–105, 2018.

[38] W. F. Giggenbach, "Geothermal solute equilibria. Derivation of Na-K-Mg-Ca geoindicators," *Geochimica et Cosmochimica Acta*, vol. 52, no. 12, pp. 2749–2765, 1988.

[39] R. O. Fournier, "Chemical geothermometers and mixing models for geothermal systems," *Geothermics*, vol. 5, no. 1–4, pp. 41–50, 1977.

[40] A. Abdelali, I. E. Nezli, R. Kechiched, S. Attalah, S. A. Benhamida, and Z. Pang, "Geothermometry and geochemistry of groundwater in the continental intercalaire aquifer, southeastern Algeria: insights from cations, silica and SO_4-H_2O isotope geothermometers," *Applied Geochemistry*, vol. 113, p. 104492, 2020.

[41] Z. H. Pang and M. Reed, "Theoretical chemical thermometry on geothermal waters: problems and methods," *Geochimica et Cosmochimica Acta*, vol. 62, no. 6, pp. 1083–1091, 1998.

[42] J. Li, G. Sagoe, X. Wang, and Z. Yang, "Assessing the suitability of lithium-related geothermometers for estimating the temperature of felsic rock reservoirs," *Geothermics*, vol. 89, p. 101950, 2021.

[43] K. Wang, C. Hua, L. Ren et al., "Geochemical and isotopic characteristics of two geothermal systems at the Nanpu Sag, Northern Bohai Bay Basin," *Frontiers in Earth Science*, vol. 10, p. 374, 2022.

[44] Q. Guo, Z. Pang, Y. Wang, and J. Tian, "Fluid geochemistry and geothermometry applications of the Kangding high- temperature geothermal system in eastern Himalayas," *Applied Geochemistry*, vol. 81, pp. 63–75, 2017.

[45] P. Wang, X. Chen, L. Shen, K. Wu, M. Huang, and Q. Xiao, "Geochemical features of the geothermal fluids from the Mapamyum non-volcanic geothermal system (Western Tibet, China)," *Journal of Volcanology and Geothermal Research*, vol. 320, pp. 29–39, 2016.

[46] H. M. Tang and B. T. Pan, "The mechanism of Xiatang warm spring and its relation to Checun-Lushan fault," *Earth Science*, vol. 14, no. 2, pp. 173–180, 1989.

[47] B. T. Pan and H. M. Tang, "The prediction of induced seismicity in Xiatang reservoir, Henan," *Earth Science*, vol. 14, no. 2, pp. 145–154, 1989.

[48] Q. Wang, *Hydrogochemical characteristics and formation mode of the five thermal springs in Lushan County, Henan*, China University of Geosciences, Beijing, 2012.

[49] H. Craig, "Standard for reporting concentrations of deuterium and oxygen-18 in natural waters," *Science*, vol. 133, no. 3467, pp. 1833-1834, 1961.

[50] S. Pan, Y. Kong, K. Wang et al., "Magmatic origin of geothermal fluids constrained by geochemical evidence: implications for the heat source in the northeastern Tibetan Plateau," *Journal of Hydrology*, vol. 603, article 126985, 2021.

[51] W. Liu, L. Guan, Y. Liu et al., "Fluid geochemistry and geothermal anomaly along the Yushu-Ganzi-Xianshuihe fault system, eastern Tibetan Plateau: implications for regional seismic activity," *Journal of Hydrology*, vol. 607, article 127554, 2022.

[52] J. Li, L. Zhang, C. Ruan, G. Tian, G. Sagoe, and X. Wang, "Estimates of reservoir temperatures for non-magmatic convective geothermal systems: insights from the Ranwu and Rekeng geothermal fields, western Sichuan Province, China," *Journal of Hydrology*, vol. 609, article 127668, 2022.

[53] X. Wang, G. Lu, and B. X. Hu, "Hydrogeochemical characteristics and geothermometry applications of thermal waters in Coastal Xinzhou and Shenzao geothermal fields, Guangdong, China," *Geofluids*, vol. 2018, Article ID 8715080, 24 pages, 2018.

[54] Y. Wang, "*A research on geochemical characteristics of geothermal fluids in Southeast Yunnan Province, China*," Institute of Geophysics, China Earthquake Administration, 2021.

[55] W. F. Giggenbach, "Carbon-13 exchange between CO_2 and CH_4 under geothermal conditions," *Geochimica et Cosmochimica Acta*, vol. 46, no. 2, pp. 159–165, 1982.

[56] J. X. Li, Q. H. Guo, and Y. X. Wang, "Evaluation of temperature of parent geothermal fluid and its cooling processes during ascent to surface: a case study in Rehai geothermal field, Tengchong," *Earth Science*, vol. 40, no. 9, pp. 1576–1584, 2015.

[57] L. Chen, T. Ma, Y. Du et al., "Hydrochemical and isotopic (^{2}H, ^{18}O and ^{37}Cl) constraints on evolution of geothermal water in coastal plain of Southwestern Guangdong Province, China," *Journal of Volcanology and Geothermal Research*, vol. 318, pp. 45–54, 2016.

[58] J. Guo, X. Mao, S. Tong, and L. Feng, "Using hydrochemical geothermometers to calculate exchange temperature of deep geothermal system in west coastal area of Guangdong Province," *Earth Science – Journal of China University of Geosciences*, vol. 41, no. 12, pp. 2075–2087, 2016.

[59] A. H. Truesdell, M. Nathenson, and R. O. Rye, "The effects of subsurface boiling and dilution on the isotopic compositions of Yellowstone thermal waters," *Journal of Geophysical Research*, vol. 82, no. 26, pp. 3694–3704, 1977.

[60] S. Arnórsson, E. Gunnlaugsson, and H. Svavarsson, "The chemistry of geothermal waters in Iceland. III. Chemical geothometry in geothermal investigations," *Geochimica et Cosmochimica Acta*, vol. 47, no. 3, pp. 567–577, 1983.

[61] Y. K. Kharaka and R. H. Mariner, "Chemical geothermometers and their application to formation waters from sedimentary basins," in *Thermal History of Sedimentary Basins*, vol. 10, pp. 99–117, UNU Geothermal Training Program Reykjavik, Iceland, 1989.

[62] Y. K. Kharaka, M. S. Lico, and L. M. Law, "Chemical geothermometers applied to formation waters, Gulf of Mexico and California basins: ABSTRACT," *The American Association of Petroleum Geologists Bulletin*, vol. 66, no. 5, p. 588, 1982.

[63] R. O. Fournier, *Application of water geochemistry to geothermal exploration and reservoir engineering; Chap. 4. in [J]*, pp. 109–143, Geothermal systems: Principles and Case Histories, 1981.

[64] S. Arnórsson and A. Andrésdóttir, "Processes controlling the distribution of boron and chlorine in natural waters in Iceland," *Geochimica et Cosmochimica Acta*, vol. 59, no. 20, pp. 4125–4146, 1995.

[65] R. O. Fournier, *Lectures on Geochemical Interpretation of Hydrothermal Waters*, UNU Geothermal Training Programme, Reykjavik, Iceland, 1989.

[66] S. Arnórsson and A. Andrésdóttir, "Assessment of feldspar solubility constants in water in the range of 0 degrees to 350 degrees C at vapor saturation pressures," *American Journal of Science*, vol. 299, no. 3, pp. 173–209, 1999.

[67] D. L. Parkhurst and C. A. J. Appelo, *User's guide to PHREEQC-A computer program for speciation, reaction-path, 1D-transport, and inverse geochemical calculations*, US Geological Survey Water-Resources Investigations Technical Report, 1999.

[68] Z. P. Pang, "The FixAl method applied to Zhangzhou geothermal system (2), Southeast China," in *Advances in Solid Earth Sciences*, Z. H. Pangetal, Ed., pp. 144–153, Science Press, 1996.

[69] R. O. Fournier, "Geochemical and hydrologic considerations and the use of enthalpy-chloride diagrams in the prediction of underground conditions in hot-spring systems," *Journal of Volcanology and Geothermal Research*, vol. 5, no. 1–2, pp. 1–16, 1979.